ACS APPLIED MATERIALS & INTERFACES

Research Article

www.acsami.org

Photoluminescence (PL) Quenching and Enhanced Photocatalytic Activity of Au-Decorated ZnO Nanorods Fabricated through Microwave-Assisted Chemical Synthesis

Ma. De Lourdes Ruiz Peralta, U. Pal,* and R. Sánchez Zeferino

Instituto de Física, Benemérita Universidad Autónoma de Puebla, Apdo. Postal J-48, Puebla, Pue. 72570, Mexico

ABSTRACT: ZnO nanorods decorated with gold nanoparticles of ~20 nm average size were fabricated by microwave-assisted chemical synthesis. For the surface-attached growth of metal nanoparticles, the ZnO nanostructures were first functionalized by sodium citrate and then the metal ions were reduced under microwave heating. While the incorporation of gold nanoparticles at the surface seen to quench both the band edge and visible emissions of the ZnO nanostructures, it enhances the degradation rate of Rhodamine 6G up to 3 folds under UV emission. The mechanisms of citrate functionalization, growth of Au nanoparticles on the surface of the oxide nanostructures, luminescence emission quenching, and enhanced photocatalytic activity of the composite nanostructures have been discussed.

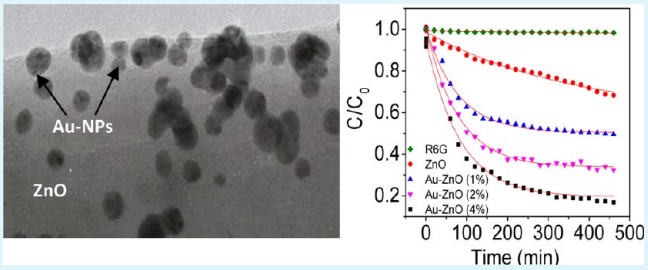

KEYWORDS: *zinc oxide, metal-semiconductor nanocomposite, microwave synthesis, photoluminescence, photocatalysis*

1. INTRODUCTION

Recent enhanced interest on metal−ZnO nanocomposites (NCs) fabricated by incorporating noble-metal nanoparticles (NPs) onto the surface of ZnO nanostructures is due to their unique optical and electronic properties.[1−3] For example, gold nanoparticles attached to ZnO nanowires have been observed to quench the green emission and enhance the UV emission of ZnO in photoluminescence (PL).[4] The UV/green emission ratio could be reversibly and reproducibly tailored by attaching or detaching the Au NPs. ZnO nanorods decorated with gold nanoparticles have also been successfully utilized as glucose biosensors[5] and photoelectrodes in dye-sensitized solar cells (DSSC).[6] On the other hand, Au-ZnO NCs prepared by modifying ZnO surface with preformed Au nanoparticles protected with bifunctional glutathione ligand have been utilized for the degradation of organic pollutants, exhibiting strong photocatalytic activity.[7]

Generally, one-dimensional (1-D) metal−ZnO nanocomposites are fabricated by growing or attaching metal NPs onto the surface of prefabricated 1-D ZnO nanostructures. For this purpose, several methods, such as sol−gel,[8] hydrothermal,[9] chemical reduction,[10] and flame spray pyrolysis,[11] have been utilized. However, most of these synthesis methods utilize conventional heating to initialize the nucleation process at high temperature, followed by controlled precursor addition to the reaction mixture. The reaction vessel acts as an intermediary for the energy-transfer process from the heating source to the reactant molecules, which can cause sharp thermal gradients throughout the bulk solution and turn out to be inefficient, because of nonuniform reaction conditions.[12] On the other hand, microwave heating method provides rapid and uniform heating of reagents and solvents. It has the advantages of homogeneous volumetric heating, high reaction rate and selectivity, and energy savings, compared with conventional heating methods.[13,14]

In this work, we report on the microwave-assisted chemical synthesis of ZnO nanorods, 1-D Au-ZnO nanocomposites, and their photocatalytic behaviors for the degradation of Rhodamine 6G (R6G). The surfaces of the ZnO nanorods were functionalized with sodium citrate to reduce Au ions over them under microwave irradiation. The influences of functionalization time and the concentration of Au precursor in the reaction mixture on the formation of Au nanoparticles, their size, and density over the nanorod surface have been studied. The mechanism of formation of Au nanoparticles over the citrate-functionalized ZnO surface, i.e., the formation of Au/ZnO heterocontacts, their luminescence quenching, and photocatalytic behaviors for R6G degradation have been discussed.

2. EXPERIMENTAL SECTION

2.1. Synthesis of ZnO Nanorods. The details of the ZnO nanorod synthesis process has been described in our previous report.[15] Briefly, 160 mL of an 8×10^{-3} M zinc nitrate hexahydrate aqueous solution was added to 160 mL of 8×10^{-3} M hexamine aqueous solution under magnetic stirring. The pH of the mixture solution was adjusted to 5.5 by dropwise addition of 1.0 M sodium hydroxide solution. The resultant solution was introduced into a domestic microwave oven (LG, Model SVMS 0745VS) and irradiated for 50 min (5 cycles of 10 min with ~10 min pause after each cycle) with 475 W of microwave power. Finally, the white product was separated and washed several times with ethanol through centrifugation.

Received: June 25, 2012
Accepted: August 31, 2012
Published: August 31, 2012

   dx.doi.org/10.1021/am301155u | *ACS Appl. Mater. Interfaces* 2012, 4, 4807−4816

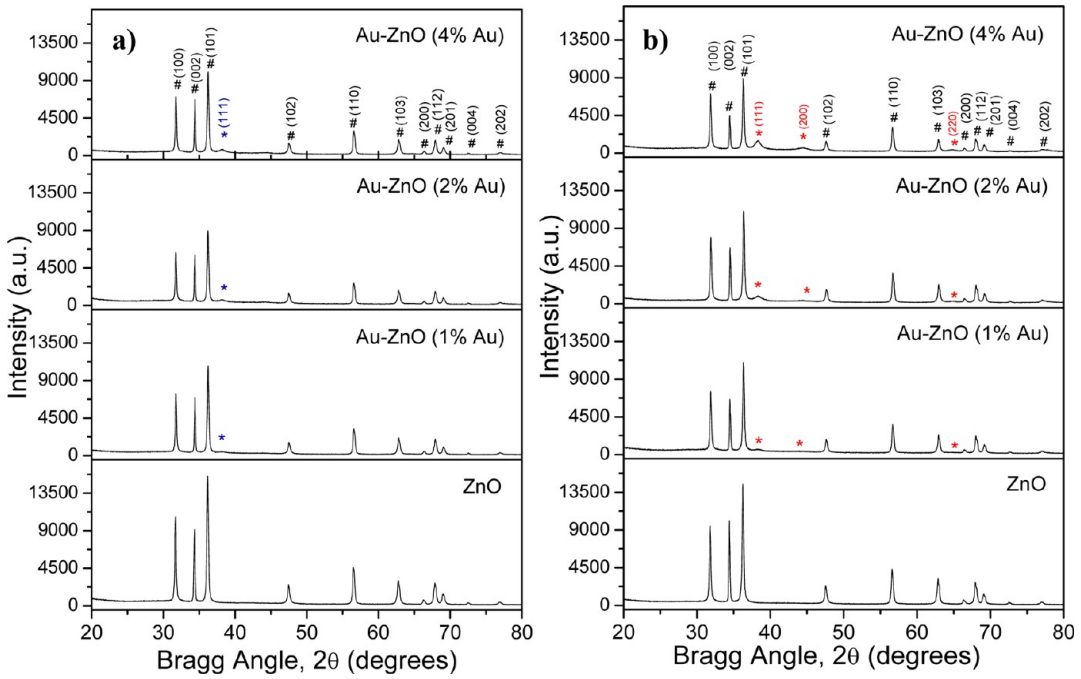

Figure 1. XRD patterns of ZnO and Au-ZnO nanocomposites citrate functionalized for (a) 1 h and (b) 12 h.

2.2. Synthesis of Au-ZnO Nanocomposites. Au-ZnO NCs with different nominal molar percentages of Au were synthesized by growing Au NPs over the surface of ZnO nanorods through microwave-assisted chemical reduction of Au ions. For the synthesis of Au-ZnO nanocomposites with nominal 1.0 mol % of Au, first, the surface of the synthesized ZnO nanorods was functionalized with sodium citrate dihydrate ($Na_3C_6H_5O_7{\cdot}2H_2O$, Sigma–Aldrich, 99%). For this purpose, ~100 mg of as-prepared ZnO nanorods were redispersed in 150 mL of deionized (DI) water and a 5 mL of sodium citrate dihydrate solution (0.11 M) was added to it. The mixture was kept under vigorous magnetic stirring for different durations (1, 6, or 12 h) at room temperature. Five milliliters (5 mL) of aqueous hydrogen tetrachloro-aurate(III) trihydrate ($HAuCl_4{\cdot}3H_2O$, Sigma–Aldrich, 99.9%) solution (2.6 mM) was added to the reaction mixture and stirred for another 15 min. The resulting mixture solution in glass beaker was introduced into the microwave oven and irradiated for 10 min with 475 W of microwave power. The irradiation process was repeated for two cycles. The maximum temperature of the reaction mixture reached to 95 °C. After two cycles of microwave irradiation, the reaction mixture was cooled to room temperature and the precipitates were separated from the solution by centrifugation, washed with DI water and ethanol several times, and finally dried at room temperature obtaining violet-colored powders. The Au-ZnO NCs with nominal Au contents of 2.0 and 4.0 mol % were fabricated under the same conditions, maintaining the molar ratio between sodium citrate and gold salt fixed (sodium citrate/gold salt = 1:11).

2.3. Characterization of ZnO and Au-ZnO. The crystalline phases of the ZnO and Au-ZnO composite samples were identified by X-ray diffraction (XRD) using the Cu Kα emission (λ = 1.5406 Å) of a Bruker Discover D8 diffractometer. The morphology of the samples was inspected in a JEOL Model JSM6610LV field-emission scanning electron microscopy (FE-SEM) system. Transmission electron microscopy (TEM) measurements on the samples were carried out using a JEOL Model JEM2100 microscope operating at 200 kV. For the TEM observations, the samples were prepared by placing a drop of the colloidal sample solution on a carbon-coated copper grid and drying at room temperature. To study the functionalization process of the ZnO nanorods, Fourier transform infrared (FT-IR) spectra of the samples were recorded before and after the functionalization process in a Vertex 70 Bruker spectrometer. Raman spectra of the samples were collected using an Olympus Model BX41 micro-Raman system of Horiba Jobin–Yvon, coupled with a thermoelectrically cooled charge-coupled detector (CCD). A He–Ne (λ = 532.6 nm) laser was used as excitation source. Room-temperature photoluminescence (PL) spectra of the samples were measured using a 0.5-m-long 9040 ScienceTech monochromator coupled with a Hamamatsu PMH-04 photomultiplier. The 325-nm emission of a He–Cd laser source (Melles Griot) of 10 mW power was used for exciting the samples.

2.4. Photocatalytic Evaluation of ZnO and Au-ZnO Nanocomposites. Rhodamine 6G was employed as a representative dye pollutant to evaluate the photocatalytic activity of ZnO and Au-ZnO samples for its degradation. For the photocatalytic studies, a mixture of 50 mL of R6G aqueous solution (10 ppm) and 50 mg of catalyst powder (ZnO or Au-ZnO nanocomposite) were mixed under magnetic stirring for 30 min in a glass beaker in the dark. The mixture solutions were kept under atmospheric conditions and air flow, without further agitation.

To monitor the degradation process, the absorption spectra of R6G solutions and the R6G solution with ZnO or Au-ZnO were recorded with a Varian Cary100 UV–vis spectrophotometer coupled with a coaxial optical fiber, which acted as the excitation source as well as collector of the reflected light from the dye incorporated reaction mixture during the measurement of its absorption spectra. An Hg lamp (UVP-XX-15S) with predominant 254-nm emission was utilized as the illumination source. The intensity of irradiation was ~1600 μW cm^{-2}. The absorption spectra of the reaction solutions were monitored every 20 min after ~5 min of switching off the irradiation source, to allow the suspended catalysts to precipitate.

3. RESULTS AND DISCUSSION

Figure 1 shows the XRD patterns of the ZnO nanorods and Au-ZnO nanocomposites functionalized for 1 and 12 h. The XRD patterns of the composites revealed two sets of diffraction peaks. Strong diffraction peaks marked with a hashmark (#) match well with the standard Bragg reflections of wurtzite ZnO (JCPDS File Card No. 36-1451). In addition, there appeared to be several weak peaks marked with an asterisk (*), which could be assigned to the diffraction lines of face center cubic (fcc) gold (JCPDS File Card No. 04-9748). For the composite samples functionalized for 1 h, only the peak corresponds to the (111) plane of fcc gold was observed. However,

dx.doi.org/10.1021/am301155u | ACS Appl. Mater. Interfaces 2012, 4, 4807–4816

for the composite functionalized for 12 h, the number of diffraction peaks associated to metallic gold increased, revealing (200) and (220) planes of fcc gold.

The average crystallite sizes in the ZnO and Au-ZnO samples functionalized for 12 h (Table 1) were estimated using the Scherrer equation:[16]

Table 1. Crystallite Size of the ZnO and Au-ZnO Nanocomposites (Functionalized for 12 h)

sample	photocatalytic efficiency, η (%)
ZnO	27
1% Au-ZnO	44
2% Au-ZnO	65
4% Au-ZnO	84

$$p = \frac{0.9\lambda}{\beta \cos \theta} \quad (1)$$

where p is the average crystallite size, λ (1.5406 Å) is the wavelength of the X-ray beam, β is the full width at half-maximum (fwhm) of the diffraction peak (in radians), and θ is the Bragg angle. With the increase of nominal Au content (%) in the composites, while the average crystallite size of ZnO did not vary significantly, the average crystallite sizes of the formed Au nanoparticles increased.

Figure 2 shows a typical SEM image of the as-prepared ZnO sample, clearly revealing the formation of rodlike nanostructures

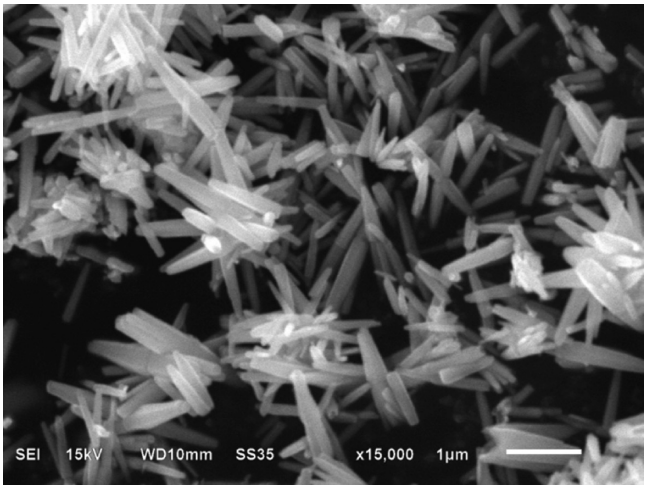

Figure 2. Typical SEM image of ZnO nanorods prepared by microwave-assisted chemical synthesis.

of faceted surface planes, with an average diameter of 162 nm and an average length of 1.27 μm. The SEM images of the Au-ZnO nanocomposites synthesized at different functionalization times (1, 6, and 12 h) are presented in Figure 3. The formation of Au nanoparticles on the surface of ZnO nanorods is evident from the SEM images. As can be seen from the images, upon increasing the content (mol %) of Au, the number of Au nanoparticles decorated on the surface of the ZnO nanorods increases, and their sizes also varies slightly.

Typical TEM images of the nanocomposites containing different nominal contents (%) of Au prepared with 6 h of functionalization time are presented in Figure 4. Formation of Au nanoparticles (NPs) on the surface of ZnO nanorods is very much clear from the micrographs. From the size distribution histograms presented as the insets of the figure, we can see the average size of the formed Au NPs was almost same for all the NCs (~21.8, 19.9, and 20.5 nm for the Au-ZnO NCs prepared with 1.0, 2.0, and 4.0 mol % Au, respectively). It must be noted that, lthough the average grain size of the Au NPs in the composites (Table 1) increased substantially upon increasing the concentration of Au precursor in the reaction mixture, the final size of the particles did not vary significantly. The fact can be understood upon considering the growth process of Au NPs in citrate reduction process, which includes four steps: first, the rapid formation of nuclei; then, their coalescence or Ostwald ripening into bigger particles; then, the diffusion-controlled growth of the particles from the precursor; and finally, a rapid consumption of the remaining Au(III) species resulting a rapid increase of particle size, as suggested by Plote et al.[17] In the normal resistive heating process, all the four steps complete within 50 min of the reaction at 75 °C. However, in the present case, upon using microwave heating, the rate of heating is much faster, and the final temperature of the reaction mixture reached to 95 °C within 3 min, rendering all the above-mentioned four growth steps to occur at much-faster rates. Therefore, upon increasing the Au(III) precursor in the reaction solution, the fast microwave heating caused a rapid nucleation of the reduced ions, increasing the number Au NPs over the ZnO surface through a rapid consumption of Au (III) precursor ions, without significant change in their final size.

To optimize the functionalization time, FT-IR spectra were recorded for the as-grown ZnO nanorods and ZnO nanorods citrate functionalized for 1 and 12 h (Figure 5). The FT-IR spectrum of the as-grown ZnO sample revealed two absorption bands localized at ~2350 cm^{-1} and 530 cm^{-1}, along with a broad weak band at ~3400 cm^{-1} associated to the water molecules adsorbed at the sample surface.[18] While the IR band located at ~2350 cm^{-1} corresponds to the O═C═O asymmetric stretching vibrational mode of CO_2 present in the atmosphere,[19] the 530 cm^{-1} band could be assigned to the stretching vibration of the Zn−O bond in ZnO lattice.[20,21] While the feature of the FT-IR spectrum did not change much for the ZnO nanorods functionalized for 1 h, it changed drastically upon increasing the functionalization time to 12 h. The FT-IR spectrum of the 12 h citrate functionalized ZnO sample revealed five additional prominent absorption bands located at ~714, 901, 1393, 1557, and 3400 cm^{-1}, in addition to the bands associated to ZnO, CO_2, and water. The absorption bands located at 1557 and 1393 cm^{-1} are attributed to the asymmetric (υ_{as}) and symmetric stretching (υ_s) vibrations of carboxyl group (COO^-) of sodium citrate, respectively.[22] Several authors have considered the magnitude of separation (Δ) between the symmetric and asymmetric vibrations of the COO^- group as a measure for the coordination structure. In general, for a monodentate ligand, the magnitude of separation Δ is higher than 200 cm^{-1}. On the other hand, Δ < 110 cm^{-1} is expected for the COO^- groups coordinated as bidentate chelate. For a bridging ligand, Δ should be between 140 and 200 cm^{-1}.[23,24] In the present case, the ZnO nanorods functionalized for 12 h revealed Δ = 164 cm^{-1}, which indicates that the ligand configuration in the sample is a bridging configuration. The absorption bands located at ~901 and 714 cm^{-1} have been tentatively assigned to the stretching vibration of C−C and rocking vibration of CH_2 groups of the citrate, respectively.[25] Finally, the broad band located at 3400 cm^{-1} was attributed to the stretching vibrational mode of O−H associated to the water molecules adsorbed

dx.doi.org/10.1021/am301155u | ACS Appl. Mater. Interfaces 2012, 4, 4807−4816

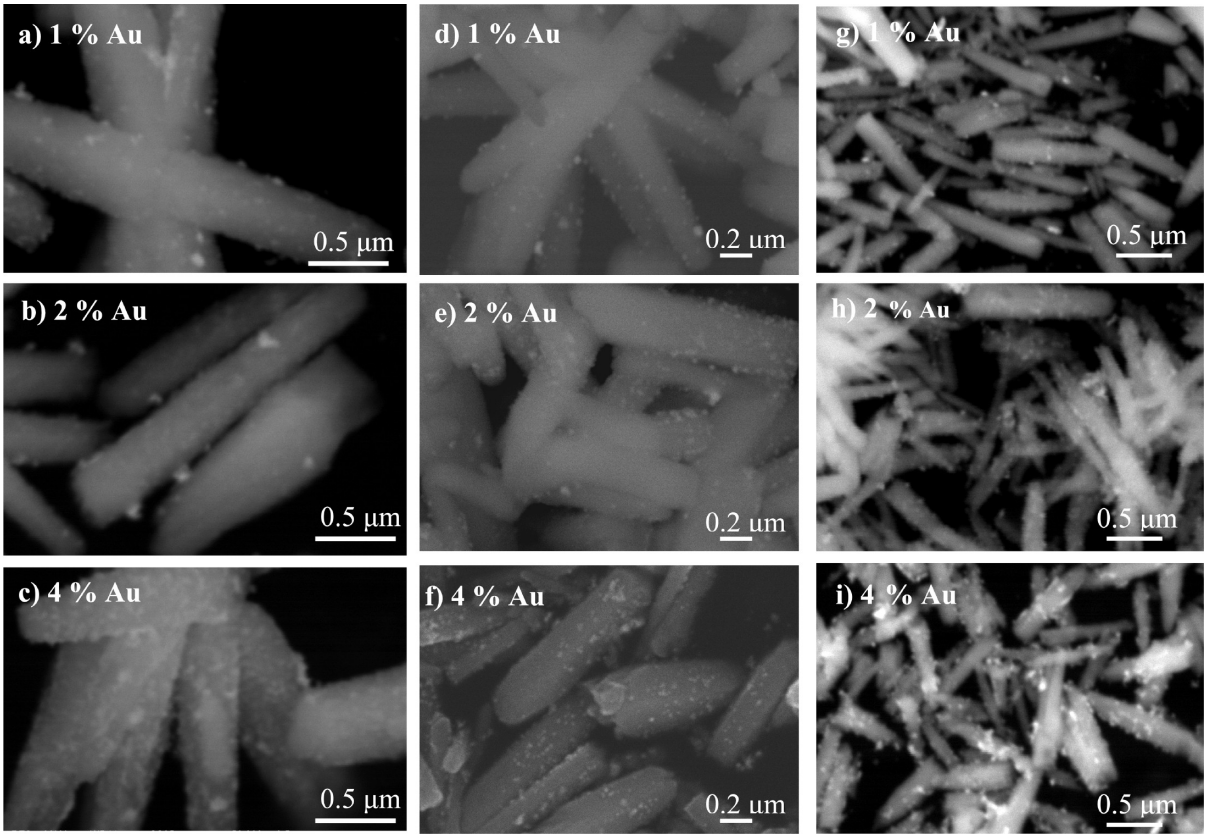

Figure 3. High-magnification SEM images of the as-prepared nanocomposites with different gold contents, functionalized for (a–c) 1 h (left column), (d–f) 6 h (center column), and (g–i) 12 h (right column).

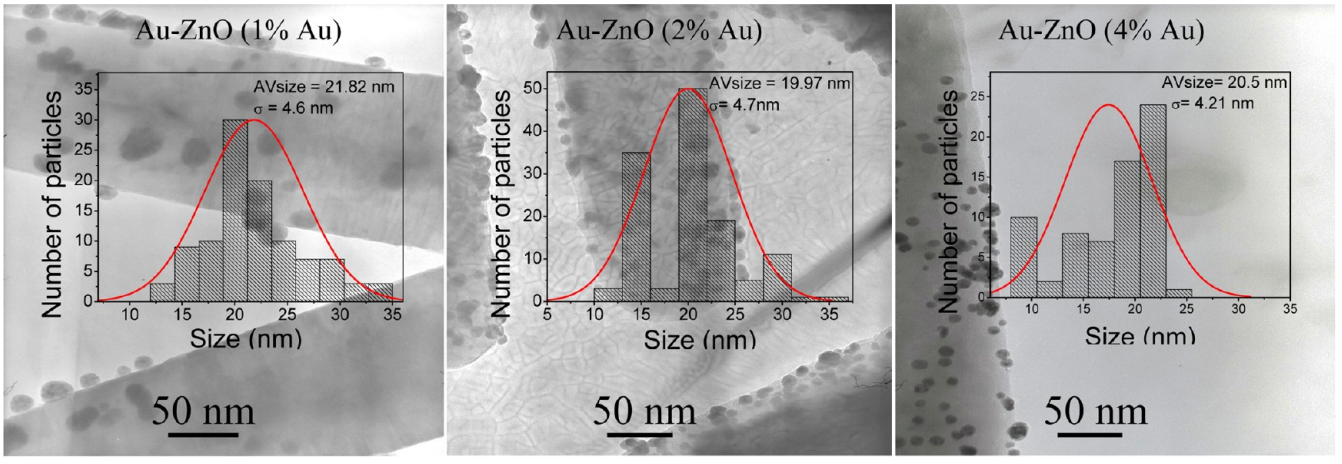

Figure 4. Typical TEM images of Au-ZnO nanocomposites prepared with different Au contents: (a) 1% Au, (b) 2% Au, and (c) 4% Au, showing the formation of a large number of Au NPs over them. The insets present the size distribution histograms of the Au NPs in each sample.

on the surface of ZnO.[18] As has been mentioned earlier, the IR spectrum of the ZnO nanorods functionalized for 1 h did not reveal the bands associated to C–C and COO^- groups clearly, which indicates the time of functionalization (1 h) was insufficient. On the other hand, the presence of those bands with high intensity in the sample functionalized for 12 h indicates that the functionalization time might be excessive. Therefore, we considered a 6-h time of functionalization as being optimum for the incorporation of Au NPs over the surface of the ZnO nanorods. In fact, the ZnO nanorods functionalized with sodium citrate for 6 h revealed very similar FT-IR spectrum to the nanorods functionalized for 1 h (not shown), and all the further measurements were performed on them.

The FT-IR spectra of the composite samples indicate that the functionalization process occurs in several steps. First, the sodium citrate molecules get ionized (eq 2) in an aqueous medium, and then the citrate ions get bonded with the Zn atoms of ZnO (eq 3) by chelating through bridging between the Zn atoms and the carboxyl group of citrate.[26] Upon adding the Au precursor into the solution, the Au ions get reduced to Au atoms over the ZnO surface.[27,28] In the first step of the reduction

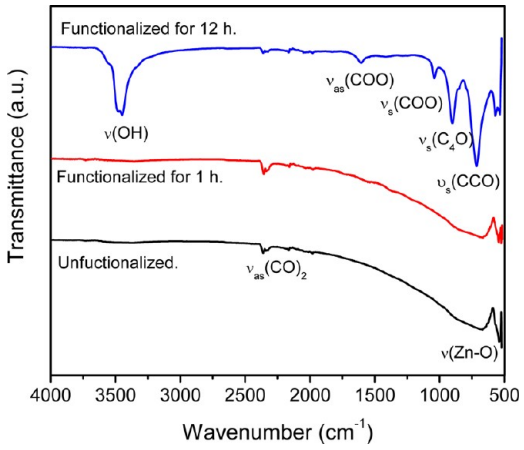

Figure 5. IR spectra of ZnO nanorods citrate, functionalized for different periods. Appearance of the symmetrical and asymmetrical vibrational modes of COO^- group confirms the coordination of citrate with ZnO.

process, the sodium citrate is oxidized to dicarboxy acetone (eq 4). The second step is the reduction of the auric salt to aurous salt (eq 5b). The last step is the disproportionation of aurous species to Au atoms (eq 6).[29] Finally, the Au-ZnO nanocomposites were formed by the growth of Au nanoparticles onto the ZnO surface.

$$Na_3C_6H_5O_7{\cdot}2H_2O + H_2O \longrightarrow (C_6H_5O_7)^{-3} + 3Na^+ + 3H_2O \quad (2)$$

$$4Zn^{2+} + (C_6H_5O_7)^{-3} \longrightarrow$$

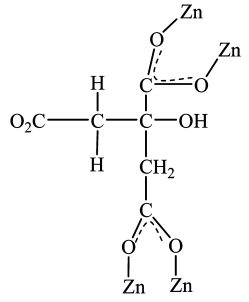

(3)

$$HAuCl_4{\cdot}3H_2O + H_2O \longrightarrow AuCl_3 + HCl + 4H_2O \quad (5a)$$

$$AuCl_3 + 2e^- \longrightarrow AuCl + 2Cl^- \quad (5b)$$

$$3AuCl \longrightarrow 2Au^o + AuCl_3 \quad (6)$$

The composite samples prepared by functionalizing ZnO nanorods for 6 h were studied through micro-Raman spectroscopy and photoluminescence. As ZnO crystallizes in a hexagonal wurtzite structure with C_{6v}^4 symmetry, the group theory predicts the presence of eight sets of phonon modes at the Γ point of its Brillouin zone:[30]

$$\Gamma = 2A_1 + 2B_1 + 2E_1 + 2E_2 \quad (7)$$

The fundamental A_1 and E_1 modes are polar in nature, both infrared and Raman active, and split into transverse and longitudinal optical (TO and LO) components. The nonpolar mode E_2 with two components E_{2L} and E_{2H} is only Raman-active. While the component E_{2L} is associated with the vibration of Zn atoms in the ZnO lattice, the E_{2H} component correspond to the vibration of the O atoms in ZnO lattice. Finally, the B_1 modes, associated with lattice disorders, are active both in Raman and infrared, and commonly designated as silent modes in ZnO.[31,32]

In Figure 6, the room-temperature Raman spectra of the ZnO and Au-ZnO samples containing different Au contents are

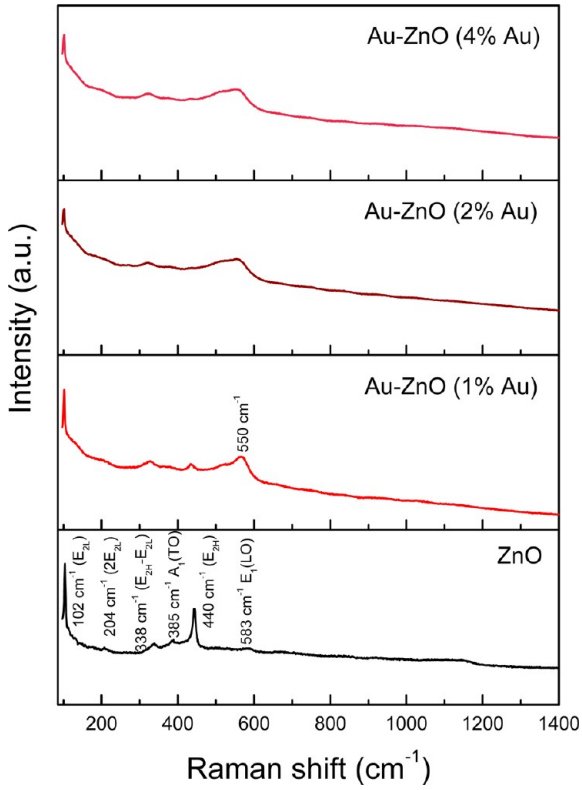

Figure 6. Micro-Raman spectra of Au-ZnO nanocomposites prepared using ZnO nanorods functionalized for 6 h.

presented. As can be seen, an intense, asymmetric broad band appeared at ~550 cm^{-1} for all the composite samples. The band has been assigned to the silent mode in ZnO.[33] Upon computer deconvolution, the broad band revealed that two components (Figure 7) peaked at ~520 cm^{-1} and 560 cm^{-1}. The two components could be assigned to the $2B_{2L}$ and B_{1L} silent modes of ZnO, respectively.[33] In general, two possible mechanisms are considered to delineate the origin of anomalous (silent) modes: disorder-activated scattering or local lattice vibration.[34] The disorders (caused by defects or impurities) in the crystal result in the breakdown of the translational symmetry of the periodic lattice, which yields a partial relaxation of the $q = 0$ selection rule for the first- and second-order Raman scattering, so the phonons from the entire Brillouin zone can be observed.[35,36]

Apart from the silent modes, there appeared a prominent Raman peak at ~102 cm^{-1} and several weak bands at ~204, 338, 385, and 440 cm^{-1} for all the samples. While the 102 cm^{-1} peak is the fundamental nonpolar $2E_{2L}$ mode, the bands appeared at ~204 and 338 cm^{-1} could be assigned to the $2E_{2L}$ and $E_{2H}-E_{2L}$ modes associated with multiphonon processes, respectively.[37] Finally, the bands appeared around 385 and 400 cm^{-1} were assigned to the transverse optical (TO) component of the fundamental A1 mode, and the E_{2H} multiphonon modes, respectively. The small hump appeared at ~580 cm^{-1} exclusively for the functionalized ZnO nanorods could be assigned to the longitudinal optical (LO) component of the fundamental E1 mode of ZnO associated with defects such as oxygen vacancy, zinc interstitial,

dx.doi.org/10.1021/am301155u | ACS Appl. Mater. Interfaces 2012, 4, 4807−4816

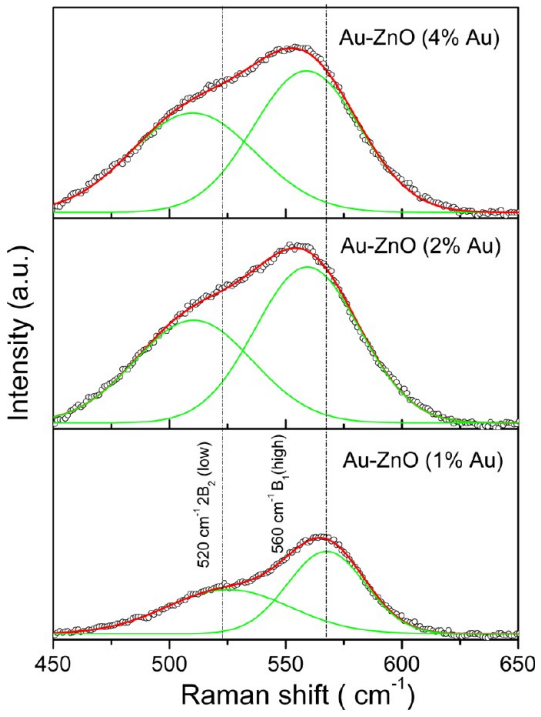

Figure 7. Expanded micro-Raman spectra of Au-ZnO nanocomposites (functionalized for 6 h) with computer-deconvoluted Raman bands.

or their complexes.[38,39] It must be noted that there appeared no Raman band associated with either citrate or dicarboxy acetone derived from its oxidation[40] in these samples, supporting our previous consideration of the optimum functionalization time being 6 h.

Figure 8 presents the room-temperature PL spectra of the ZnO and Au-ZnO nanocomposites containing different Au contents. All the spectra revealed two emission bands located at ~385 and 585 nm. While the sharper 385-nm emission band has been commonly assigned as the near-band-edge emission in ZnO,[41] the band in the visible spectral range (peaked at ~585 nm) has been attributed to the recombination of photogenerated holes with singly ionized charge states of the intrinsic defects such as oxygen vacancies, Zn interstitials, or impurities.[42−45]

The characteristics of the PL spectra of the Au-ZnO nanocomposites were very similar to ZnO without Au nanoparticles. However, the intensity of both the emission bands in these cases was much lower, indicating a quenching of PL emissions due to the incorporation of Au NPs on ZnO surface. A similar of PL quenching effect has been reported for CdSe quantum dots functionalized with Au nanoparticles in aqueous media,[46] and attributed to the electron transfer process from the electronic orbitals below the Fermi level of gold to the deep hole trap of CdSe quantum dots. On the other hand, both an enhancement and quenching of PL emission have been reported for the ZnO/Ag_2O nanocomposites.[47] The emission enhancement in ZnO/Ag_2O has been explained through the interaction between the Ag_2O nanoparticles and surface defects of the matrix, which changes the defect structures, leading to the passivation of deep defect activities. The reduction of surface defects in these composites enhances the number of energetic electrons in the conduction band to recombine with the holes in the valence band, causing an

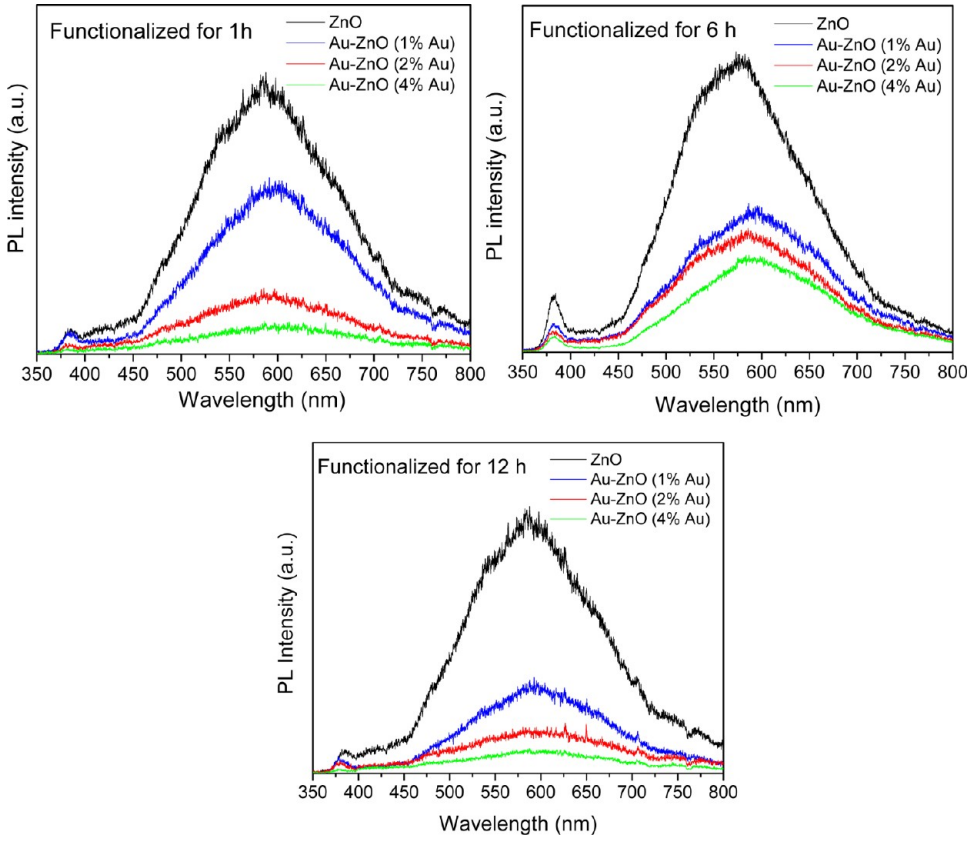

Figure 8. PL spectra of the Au-ZnO nanocomposites fabricated using ZnO nanorods functionalized for different periods.

enhancement of the near band-edge emission. On the other hand, when the number of Ag_2O nanoparticles over the ZnO surface increases, or their size increases (increasing the filling factor over the CdSe surface), the intensity of the near band-edge emission gets reduced.[47]

For the semiconductor ZnO, when excited by photons of energy equal to or higher than its band gap, electrons in the valence band (VB) can be excited to the conduction band (CB) creating electron−hole pairs. However, the presence of metal NPs over the ZnO surface can alter its emission behavior through different mechanisms. Using the radiating plasmon model, Lakowicz[48] explained that the surface plasmon resonance (SPR) scattering of metal NPs can enhance the PL emission, while the surface plasmon absorption can cause a quenching. According to his observations, PL enhancement in semiconductor usually occurs on rough metal surface or metal NPs of larger sizes, and the quenching occurs on smoother metal surface or metal NPs of smaller sizes.

As has been discussed by Zhou et al.[49] for their ion-implanted Ag-ZnO thin films, the effect of plasmon resonance scattering occurs only when the energy of SPR energy of the metal NPs is higher or close to the band gap energy of the semiconductor. On the other hand, both the enhancement and quenching of PL emission can occur, depending on the nature of the electron transfer process between the metal NPs and the semiconductor.[50,51] While the PL emission, especially the band-edge emission can be enhanced due to the electron transfer from metal NPs to the semiconductor, the emission can be quenched through electron transfer from the semiconductor to the metal NPs.

The electron transfer between the semiconductor and metal NPs takes place when they are in direct contact. The direction of electron transfer between them depends on the band structures of the semiconductor and the metal, as well as their energy states. In the present case, considering the work functions of ZnO and Au (5.4 and 5.1 eV, respectively),[52,53] we can draw the band structure of our Au-ZnO system as shown in Figure 9. Because of the larger work function of

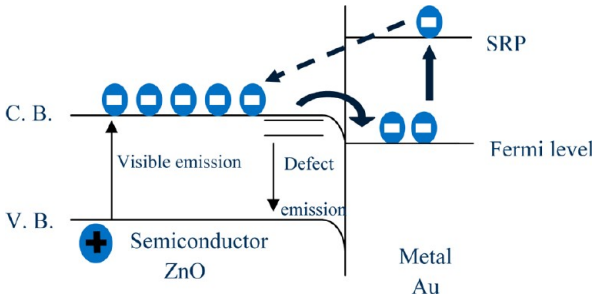

Figure 9. Schematic band diagram of a ZnO/Au heterostructure (representative of Au-ZnO nanocomposite), showing the charge distribution and PL emission processes.

ZnO, its Fermi energy level lies lower than the Fermi energy level of gold, and the initial electron transfer between the Au NPs and ZnO will cause a band bending. Irradiation of the composite samples by He−Cd laser will excite the free electrons of Au NPs to a higher energy state (Figure 9), which is higher than the CB edge of ZnO. Although these excited electrons would be transferred to the CB of ZnO situated at lower energy, they will be easily transferred back to the Fermi energy level of the Au NPs, as it is situated below the CB edge of ZnO. These phenomena would result in a quenching of the band-edge emission of ZnO in its PL spectrum.

On the other hand, electrons from the CB of ZnO can also be transferred to the Au NPs in contact, causing an increase in their electron density. The high-density electrons of the Au NPs can be transferred to the defect levels of ZnO if they are situated below the Fermi level of Au, causing an enhancement of defect emission. However, since the work function of Au is high enough, its Fermi energy level should lie below most of the defect levels of ZnO, casing a quenching of defect emission. A similar observation has also been made for the ZnO/Au system by Li et al.[54] It must be noted that the average sizes of the Au NPs in all our composite samples are small (≤21.0 nm); therefore, absorption dominates over the scattering process, for which the radiating plasmon model of Lakowicz[48] also predicts a PL quenching.

As the Au NPs on the surface of ZnO nanorods act as electron traps, we expected our composite samples to work as efficient photocatalysts. To verify the photocatalytic activity of the composite samples, they were tested for Rhodamine 6G degradation process under UV illumination. Rhodamine 6G reveals three absorption bands, located at 247, 275, and 526 nm in its absorption spectrum in the UV−vis spectral range. While the band in the visible region (526 nm) is responsible for the chromophoric components (the color of the dye arises from the aromatic rings connected by azo groups), the two UV bands (247 and 275 nm) are attributed to the absorption of benzene-like and naphthalene-like structures in the molecule, respectively.[55] To study its photodegradation behavior, we monitored the visible absorption band (526 nm) of the dye in its absorption spectra during the photocatalytic reaction process. In the absence of catalyst (ZnO or Au-ZnO), there observed no change in the intensity of the 526-nm absorption band of R6G solution upon UV illumination up to 40 min. The temporal evolution of the absorption profile during the photocatalyitic degradation of RG6 with ZnO and Au-ZnO 4.0% nanocomposite are shown in Figure 10. The reduction of

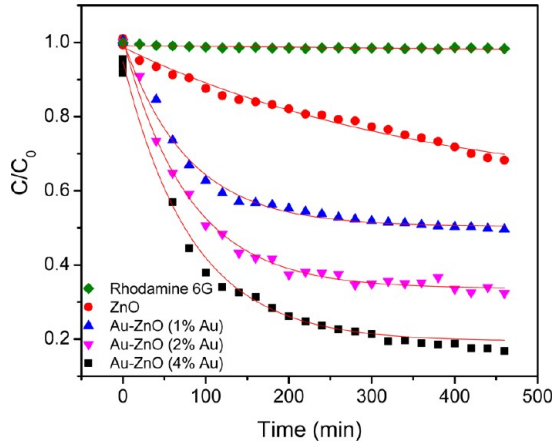

Figure 10. Kinetics of R6G photodegradation by Au-ZnO nanocomposites containing different Au contents.

intensity of the visible absorption band (525 nm) for both the samples indicates degradation of the dye. As can be seen, both ZnO and Au-ZnO show similar intensity variation pattern of the absorption profiles, suggesting a similar pathway of R6G degradation by both.[7] However, for the Au-ZnO nanocomposite, the intensity of the R6G absorption band diminished

at much faster rate, indicating its enhanced photocatalytic activity.

Figure 10 shows the decolorization curves for all the samples estimated as C/C_0 versus time, where C_0 is the initial concentration and C is the concentration of R6G at a particular time. As we can see, the photodegradation of the dye does not occur in the absence of a catalyst. On the other hand, the photocatalytic activity of ZnO nanorods is low. Only ~27% of the dye could be degraded within 450 min of UV irradiation. However, the degradation rate of R6G is enhanced upon utilizing the Au-ZnO composites as catalysts, and the degradation rate increased as the Au contents increased. The rate of decolorization was calculated as a function of the change in the absorption intensity at λ_{max} (526 nm) of the dye. The decolorization efficiency η (%) could be calculated as

$$\eta\,(\%) = \frac{C_0 - C}{C_0} \times 100 \tag{8}$$

where C_0 is the initial concentration of the dye and C is the concentration after photoirradiation.[56] The calculated values of photocatalytic efficiency for the composite samples are presented in Table 2.

Table 2. R6G Decolorization Efficiencies of ZnO and Au-ZnO Nanocomposites

sample	ZnO crystallite size (nm)	Au crystallite size (nm)
ZnO	39.0	
1% Au-ZnO	39.0	3.3
2% Au-ZnO	38.90	4.7
4% Au-ZnO	38.90	8.4

The Langmuir–Hinshelwood (L-H) model was used to evaluate the kinetics of R6G degradation. This model has been used successfully to describe the kinetics of the solid–liquid system in heterogeneous photocatalysis qualitatively.[57] In this model, the reaction rate r can be expressed as

$$r = \frac{k_1 k_2 C}{1 + k_2} \tag{9}$$

where k_1 is the apparent rate constant, k_2 is the adsorption constant, and C is the reactant concentration. In order to apply the L-H model, we must take into account that the phtocatalytic process was carried out in a batch reactor, satisfying the following condition:

$$-V\frac{dC}{dt} = \frac{mAk_1C}{1 + k_2C} \tag{10}$$

where V is the liquid volume and A is the number of adsorption sites per gram of catalyst. Integrating the left-hand side of eq 10 from $t = 0$ to $t = i$ and the right-hand side from initial concentration C_0 to final concentration C_i (at $t = i$), we will have

$$\frac{\ln(C_0/C)}{C_0 - C} = -k_2 + \frac{mAk_1k_2t}{V(C_0 - C)} \tag{11}$$

Figure 11 presents the L-H plots ($(\ln(C_0/C)/(C_0 - C)$ vs $t/(C_0 - C)$) of the R6G photodegradation process by Au-ZnO composite catalysts containing nominal 1.0 and 2.0 mol % of gold. The linear behavior of the plots indicates first-order reaction kinetics for R6G photodegradation.

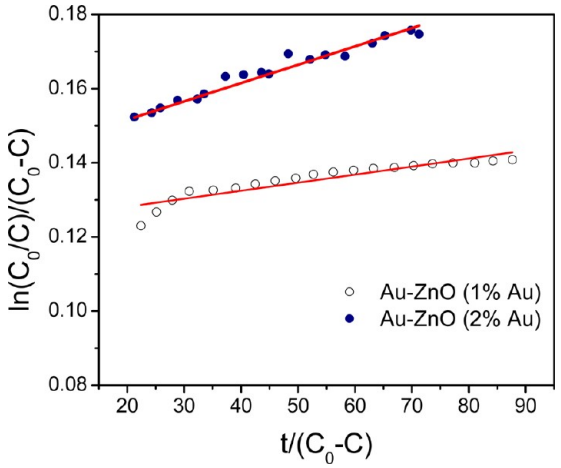

Figure 11. Langmuir–Hinshelwood (L-H) plots of the R6G photodegradation process by Au-ZnO nanocomposites.

Table 3. Apparent Rate Constant and Adsorption Constant Values Calculated Using the Langmuir–Hinshelwood Model

sample	k_1 (min^{-1})	k_2 (mg/L)
ZnO	9.74×10^{-5}	0.1157
1% Au-ZnO	2.16×10^{-4}	0.1238
2% Au-ZnO	4.94×10^{-4}	0.1257
4% Au-ZnO	1.62×10^{-3}	0.1282

Estimated k_1 and k_2 values for the samples are presented in Table 3.

Although we could not observe any significant change in the k_2 value for the nanocomposites, the value of k_1 for the nanocomposite containing 4.0 mol % Au was estimated to be of two orders of magnitude larger than that of ZnO. The enhancement can be assigned to the presence of Au NPs over the surface of ZnO nanorods, which modifies the charge separation process, resulting in great improvement of the apparent rate constant of the R6G photodegradation process.

Photocatalytic Mechanism. To understand the enhanced photocatalytic activity of Au-ZnO nanocomposites, it is necessary to evaluate the role of the metal NPs on the electronic band structure of ZnO. As has been mentioned earlier, on UV illumination, electron–hole pairs are generated in ZnO (eq 12). The photoelectrons can be trapped by electron acceptors such as adsorbed O_2 to produce superoxide radical anions ($\bullet O_2^-$) (eq 13), and the photogenerated holes can be trapped by the surface hydroxyl groups to produce hydroxyl radicals ($\bullet$OH) (eq 14). On the other hand, the photogenerated holes can dissociate water molecules in the aqueous solution, producing $\bullet$OH radicals (eq 15).[58]

$$\mathrm{ZnO} + h\nu \rightarrow h^+(\mathrm{VB}) + \mathrm{e}^-(\mathrm{CB}) \tag{12}$$

$$\mathrm{e}^- + \mathrm{O_2} \rightarrow \bullet\mathrm{O_2}^- \tag{13}$$

$$h^+\mathrm{OH}^- \rightarrow \bullet\mathrm{OH} \tag{14}$$

$$h + \mathrm{H_2O} \rightarrow \mathrm{H}^+ + \bullet\mathrm{OH} \tag{15}$$

In an aqueous medium, the R6G molecule loses the Cl atom as a free radical (eq 16):

dx.doi.org/10.1021/am301155u | ACS Appl. Mater. Interfaces 2012, 4, 4807–4816

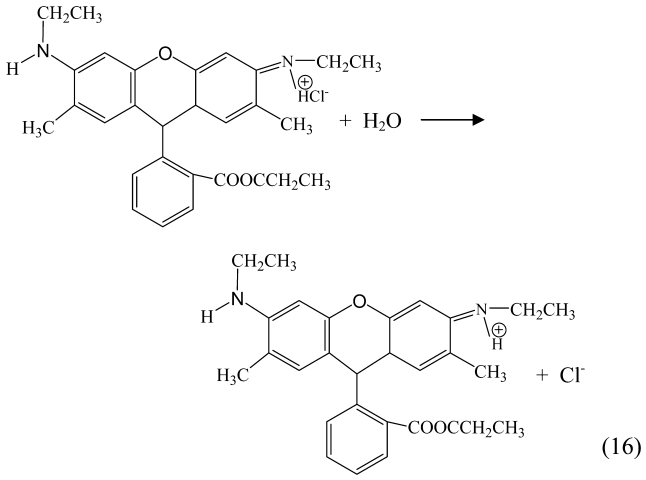

(16)

The ionized rhodamine molecule ($R6G^+$) gets oxidized by the •OH radicals (produced through eqs 14 and 15), producing colorless products (eq 17):

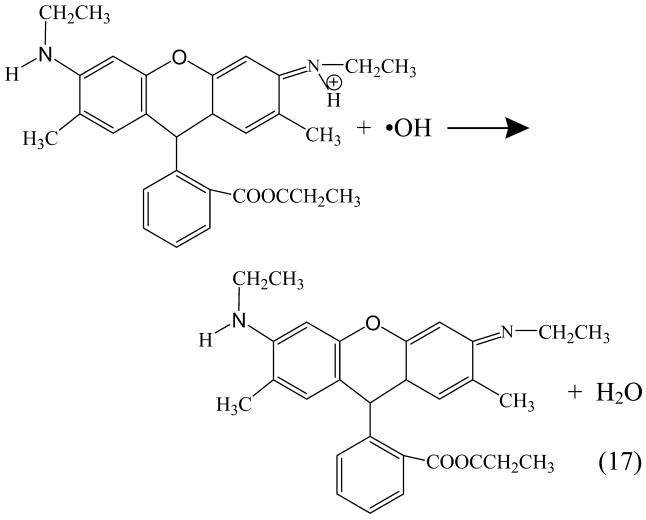

(17)

As mentioned earlier, both the holes and hydroxyl radicals are very powerful oxidants. However, the photoinduced electrons and holes can also recombine to decrease the photocatalytic efficiency. The presence of Au NPs over the ZnO nanorod surface in the composite samples causes a rapid removal of the photoinduced electrons promoted to the CB of ZnO, preventing their recombination with the holes, allowing the catalytic process to continue.[59] Therefore, the deposited Au NPs over the ZnO surface act as a reservoir of electrons, enhancing the catalytic process.[3]

As we can see from Table 3, the photocatalytic efficiency of the ZnO nanorods increases from 27 to ~87% upon incorporating Au NPs over their surfaces. However, ~400 min were needed for the catalysts to achieve such degradation. In this regard, we must mention that, during the UV-irradiation process, the catalytic mixture was not under agitation, and the degradation efficiencies were estimated from the variation of the intensity of the absorption band at 526 nm. While nonutilization of magnetic agitation exposed only a fraction of the catalyst surface to the incident UV radiation (most of the Au-ZnO NCs were precipitated at the bottom of the reaction beaker), decomposition of R6G can produce other colored intermediates with chromophore groups similar to R6G with a maximum absorbance at ~528 nm,[60] causing a lower estimation of the real degradation efficiency.

5. CONCLUSIONS

In summary, we could fabricate ZnO nanorods decorated with well-dispersed Au nanoparticles with an average size of ~20 nm over their surfaces through microwave-assisted chemical synthesis. Because of the microwave-assisted rapid heating, upon increasing the concentration of Au(III) precursor in the reaction mixture, though the number of nanoparticles (NPs) over the surface of ZnO increased, the size of the NPs does not vary significantly.

The attached Au NPs at the surface of ZnO form close contacts between the metal and the semiconductor, forming heterojunctions. The attached Au NPs act as traps for the photogenerated electron, causing the quenching of near-band-edge emission as well as defect emissions of ZnO. The electron trapping capacity of the metal NPs reduces the recombination rate of the photogenerated electrons and holes, thereby increasing the photocatalytic activity of ZnO for the degradation of Rhodamine 6G.

AUTHOR INFORMATION

Corresponding Author

*Fax: +52-222-2295611. E-mail: upal@sirio.ifuap.buap.mx.

Notes

The authors declare no competing financial interest.

ACKNOWLEDGMENTS

The work was partially supported by CONACyT, Mexico (Grant No. CB-2010/151767) and VIEP, BUAP (Grant No. VIEP/EXE/2012/137). The authors are thankful to the Department of Materials and Metallurgy, Autonomous University of Hidalgo, Mexico and Dr. E. Sánchez Mora, IFUAP, Mexico for providing the TEM and photocatalytic measurement facilities, respectively.

REFERENCES

(1) Chang, Y.; Xu, Y; Zhang, Y.; Ma, Sh.; Xin, L.; Zhu, L.; Xu, Ch. *J. Phys. Chem. C* **2009**, *113*, 18761−18767.
(2) Kamat, P. V. *J. Phys. Chem. C* **2007**, *111*, 2834−2860.
(3) Subramanian, V.; Wolf, E. E.; Kamat, P. V. *J. Phys. Chem. B* **2003**, *107*, 7479−7485.
(4) Chen, T.; Xing, G. Z.; Zhang, Z.; Chen, H. Y.; Wu, T. *Nanotechnology* **2008**, *19*, 435711(5).
(5) Wei, Y.; Li, Y.; Liu, X.; Xian, Y.; Shi, G.; Jin, L. *Biosens. Bioelectron.* **2010**, *26*, 275−278.
(6) Bora, T.; Kyaw, H. H.; Sarkar, S.; Pal, S. K.; Dutta, J. *Beilstein J. Nanotechnol.* **2011**, *2*, 681−690.
(7) Udawatte, N.; Lee, M.; Kim, J.; Lee, D. *Appl. Mater. Interfaces* **2011**, *3*, 4531−4538.
(8) Habibi, M. H.; Sheibani, R. *J. Sol−Gel Sci. Technol.* **2010**, *54*, 195−202.
(9) Lu, W.; Liu, G.; Gao, Sh.; Xing, Sh.; Wang, J. *Nanotechnology* **2008**, *19*, 445711−445720.
(10) Li, F.; Yuan, Y.; Luo, J.; Qin, Q.; Wu, J.; Li, Zh.; Huang, X. *Appl. Surf. Sci.* **2010**, *256*, 6076−6082.
(11) Height, M. J.; Pratsinis, S. E.; Mekasuwandumrong, O.; Praserthdam, P. *Appl. Catal., B* **2006**, *63*, 306−312.
(12) Gerbec, J. A.; Magana, D.; Washington, A.; Strouse, G. F. *J. Am. Chem. Soc.* **2005**, *127*, 15791−15800.
(13) Mallikarjuna, N. N.; Varma, R. S. *Cryst. Growth Des.* **2007**, *7*, 686−690.
(14) Zhu, P.; Zhang, J.; Wu, Z.; Zhang, Z. *Cryst. Growth Des.* **2008**, *8*, 3148−3153.
(15) Ruiz-Peralta, Ma.; De, L.; García-Serrano, J.; Pal, U. *Adv. Sci. Lett.* **2012**, *6*, 159−166.
(16) Cullity, B. D.; Stock, S. R. *Elements of X-Ray Diffraction*, 3rd Ed.; Prentice−Hall: Upper Saddle River, NJ, 2001; pp 167−171.

(17) Polte, J.; Ahner, T. T.; Delissen, F.; Sokolov, S.; Emmerling, F.; Thünemann, A. F.; Kraehnert, R. *J. Am. Chem. Soc.* **2010**, *132*, 1296−1301.
(18) Xiong, G.; Pal, U.; García-Serrano, J.; Ucer, K. B.; Williams, R. T. *Phys. Status Solidi C* **2006**, *3*, 3577−3581.
(19) Sandford, S. A.; Bernstein, M. P.; Allamandola, L. J.; Goorvitch, D.; Teixeira, T. C. V. S. *Astrophys. J.* **2001**, *548*, 836−851.
(20) Georgekutty, R.; Seery, M. K.; Pillai, S. C. *J. Phys. Chem. C* **2008**, *112*, 13563−13570.
(21) Bhattacharyya, S.; Gerdanken, A. *J. Phys. Chem. C* **2008**, *112*, 659−665.
(22) Wagata, H.; Ohashi, N.; Taniguchi, T.; Katsumata; Okada, K.; Matsushita, N. *Cryst. Growth Des.* **2010**, *10*, 4968−4975.
(23) Lenz, A.; Selegård, L.; Söderlindn, F.; Larrson, A.; Holtz, P. O.; Uvdal, K.; Ojamäe, L.; Käll, P. O. *J. Phys. Chem. C* **2009**, *113*, 17332−17341.
(24) Taratula, O.; Galoppini, E.; Wang, D.; Chu, D.; Zhang, Z.; Chen, H.; Saraf, G.; Lu, Y. *J. Phys. Chem. B* **2006**, *110*, 6506−6515.
(25) Marchewka, M. K.; Pietraszko, A. *J. Phys. Chem. Solids* **2003**, *64*, 2169−2181.
(26) Cho, S.; Jang, J. W.; Jung, S. H.; Lee, B. R.; Oh, E.; Lee, K. H. *Langmuir* **2009**, *25*, 3825−3831.
(27) Turkevich, J.; Stevenson, P.; Hillier, J. *Faraday Discuss.* **1951**, *11*, 55−75.
(28) Frens, G. *Nature* **1973**, *241*, 20−22.
(29) Kumar, S.; Gandhi, K. S.; Kumar, R. *Ind. Eng. Chem. Res.* **2007**, *46*, 3128−3136.
(30) Umar, A.; Karunagaran, B.; Suh, E. K.; Hahn, Y. B. *Nanotechnology* **2006**, *17*, 4072−4077.
(31) Tong, Y.; Liu, Y.; Shao, Ch.; Liu, Y.; Xu, Ch.; Zhang, J.; Lu, Y.; Shen, D.; Fan, X. *J. Phys. Chem. B* **2006**, *110*, 14714−14718.
(32) Soosen-Samuel, M.; Koshy, J.; Chandran, A.; George, K. C. *Indian J. Pure Appl. Phys.* **2010**, *48*, 703−708.
(33) Manjón, F. J.; Mari, B.; Serrano, J.; Romero, A. H. *J. Appl. Phys.* **2005**, *97*, 053516-1−053516-4.
(34) Ye, J. D.; Gu, S. L.; Zhu, S. M.; Liu, S. M.; Zhang, Y. D.; Zhang, R.; Shi, Y.; Chen, Q.; Yu, H. Q.; Ye, Y. D. *Appl. Phys. Lett.* **2006**, *88*, 101905-1−101905-5.
(35) Yadav, H. K.; Sreenivas, K.; Katiyar, R. S.; Gupta, V. *J. Phys. D: Appl. Phys.* **2007**, *40*, 6005−6009.
(36) Guo, S.; Du, Z.; Dai, S. *Phys. Status Solidi B* **2009**, *246*, 2329−2332.
(37) Calleja, J. M.; Cardona, M. *Phys. Rev. B* **2005**, *16*, 3753−3761.
(38) Mcguire, K.; Pan, Z. W.; Wang, Z. L.; Milkie, D.; Menéndez, J.; Rao, A. M. *J. Nanosci. Nanotechnol.* **2002**, *2*, 499−502.
(39) Umar, A.; Hahn, Y. B. *Nanotechnology* **2006**, *17*, 2174−2180.
(40) Munro, C. H.; Smith, W. E.; Garner, M.; Clarkson, J.; White, P. C. *Langmuir* **1995**, *11*, 3712−3720.
(41) Shi, W. S.; Cheng, B.; Zhang, L.; Samulski, E. T. *J. Appl. Phys.* **2005**, *98*, 083502-1−083502-5.
(42) Ozgour, U.; Alivov, Y. I.; Liu, C.; Teke, A.; Reshchikov, M. A.; Dogan, S.; Avrutin, V.; Cho, S. J.; Morkoc, H. *J. Appl. Phys.* **2005**, *98*, 041301-1−041301-95.
(43) Look, D. C. *Mater. Sci. Eng., B* **2001**, *80*, 383−387.
(44) Kim, T. W.; Kazawoe, T.; Yamazaki, S.; Ohtsu, M.; Sekiguchi, T. *Appl. Phys. Lett.* **2004**, *84*, 3358−3360.
(45) Qiu, Z.; Wong, K. S.; Wu, M.; Lin, W.; Xu, H. *Appl. Phys. Lett.* **2004**, *84*, 2739−2741.
(46) Nikoobakth, B.; Burda, C.; Braun, M.; Hund, M.; El-Sayed, M. A. M. *Photochem. Photobiol.* **2002**, *76*, 591−597.
(47) Lin, T. H.; Chen, T. T.; Cheng, Ch. L.; Lin, H. Y.; Chen, Y. F. *Opt. Express* **2009**, *17*, 4342−4347.
(48) Lakowicz, J. R. *Anal. Biochem.* **2005**, *337*, 171−194.
(49) Zhou, X. D.; Xiao, X. H.; Xu, J. X.; Cai, G. X.; Ren, F.; Jiang, C. Z. *Electron. Phys. Lett.* **2011**, *93*, 57009-1−57009-6.
(50) Hsieh, Y. P.; Liang, C. T.; Chen, Y. F.; Lai, C. W.; Chou, P. T. *Nanotechnology* **2007**, *18*, 1449-1−1449-4.
(51) Chen, C. W.; Wang, C. H.; Wei, C. M.; Chen, Y. F. *Appl. Phys. Lett.* **2009**, *94*, 071906-1−071906-3.
(52) Zhou, X. C.; Xiao, X. H.; Xu, J. X.; Cai, G. X.; Ren, F.; Jiang, C. Z. *Electron. Phys. Lett.* **2011**, *93*, 57009-1−57009-6.
(53) Michaelson, H. B. *J. Appl. Phys.* **1977**, *48*, 4729−4733.
(54) Li, X. H.; Zhang, Y.; Ren, X. *Opt. Express* **2009**, *17*, 8735−8740.
(55) Dükkanci, M.; Gündüz, G.; Yilmaz, S.; Prihodko, R. V. *J. Hazard. Mater.* **2010**, *181*, 343−350.
(56) Kansal, S. K.; Singh, M.; Sud, D. *J. Hazard. Mater.* **2007**, *141*, 581−590.
(57) López, T.; Hernández-Ventura, J.; Gómez, R.; Tzompantzi, F.; Sánchez, E.; Bokhimi, X.; García, A. *J. Mol. Catal. A* **2001**, *167*, 101−107.
(58) Legrini, O.; Oliveros, E.; Braun, A. M. *Chem. Rev.* **1993**, *93*, 671−698.
(59) Chang, Y.; Xu, J.; Zhang, Y.; Ma, S.; Xin, L.; Zhu, L.; Xu, C. *J. Phys. Chem. C* **2009**, *113*, 18761−18767.
(60) Menendez, A.; Lombarana, J. L. I.; De Luis, A. *J. Adv. Oxide Technol.* **2008**, *11*, 573−582.